

A Dynamic EV Charging System for Slow Moving Traffic Applications

Adeel Zaheer, Michael Neath, Hui Zhi (Zak) Beh, *Member, IEEE*, and Grant A. Covic, *Senior Member, IEEE*

Abstract— Inductive Power Transfer (IPT) is by far the most popular method to transfer energy wirelessly and has attracted considerable attention in recent times. The Wireless Power Consortium (WPC) has developed a standard (Qi) for low power consumer electronics, whereas, the Society of Automotive Engineers (SAE) is working on a standard (J2954) to charge Electric Vehicles (EVs) wirelessly. SAE's current efforts are only focused on transferring power to the vehicles at rest (static), whereas no work has been done so far on developing the standards for transferring power to the vehicles on the move (dynamic). This paper presents the magnetic design of an IPT system for a dynamic EV charging application, to continuously deliver a power of 15kW to an EV, along the direction of travel within the lateral misalignment of $\pm 200\text{mm}$. The experimental validation of system operation, however, was conducted at 5kW. The design aims at distributing the cost and complexity of the system between the primary and secondary side, while achieving a smooth power transfer profile. In addition, the system is designed to exploit the shielding effect provided by the vehicle, as the field generating components of the system are covered by the vehicle body under all operating conditions.

Index Terms— Electric Vehicles (EVs), Inductive Power Transfer (IPT), Magnetic Couplers, Magnetic analysis, Wireless charging

I. INTRODUCTION

INDUCTIVE Power Transfer (IPT) technology has come a long way in the last decade, with systems designed for specific applications (medical, domestic and industrial) [1]-[5], industrial material handling applications [6]-[9], and consumer-electronic devices [10]-[12] to Electric Vehicle (EV) charging applications [13]-[23]. IPT EV charging systems can be divided into two broad categories. Static IPT (SIPT) charging systems that are designed for charging a parked (stationary) vehicle with some level of acceptable misalignment and Dynamic IPT (DIPT) systems that are designed to deliver power to a vehicle on the move [23].

The current frontier of this technology lies at the roadway EV charging DIPT systems. Various recent works have highlighted the motivation for investigating such DIPT

systems [23]-[25]. In order to achieve power transfer on the move, the roadway has to have an embedded primary magnetic structure acting as a source of magnetic field (effectively forming a primary track) to induce power in a secondary pick-up installed underneath a vehicle. This primary track design may resemble a traditional design used for distributed (Automatic Guided Vehicle and monorail) IPT applications or may consist of a series of separate lumped pad structures. In any case, some kind of primary track segmentation scheme is implemented to ensure that only the part of the track where a vehicle is detected is energized. This paper implements the latter approach with a series of lumped pad structures (Double-D Pads or DDPs in this case [26]), intended to be deployed with a Double-Coupled System (DCS) architecture as presented in [27]. The source power supply and the load are separated by two inductive coupling links in the DCS architecture. This system architecture can be advantageous as the individual lumped pads can be designed to be smaller than the vehicle body so that, ideally, only the pad(s) underneath the vehicle may be energized upon detecting its presence, while also providing isolation between the power supply and the driven primary pads.

The system presented in this paper focuses on semi-dynamic applications such as areas around the traffic signals or taxi ranks, where it has to be designed under the assumption that the vehicles could be stacked head to tail in case of slow moving traffic. Such a dynamic charging system is required to deliver rated power to the vehicle continuously throughout the length of the track (with some tolerance to lateral displacement). In contrast, a DIPT system designed for a highway that needs to power EVs travelling at a high speed with expected significant gaps between the vehicles can be designed to deliver the required average power per unit distance.

The aim of the study presented in this paper is to develop a demonstration topology that is capable of delivering 15kW of power continuously (with a system frequency of 85 kHz) to a secondary pad installed under an EV moving along a roadway. Here, the goal was to use simple single winding pad structures in the ground (given this is likely the highest cost) and allow a more complicated multicoil pad structure on the vehicle side to help ensure continuous power transfer. The ground side is accomplished using multiple DDPs to form the primary magnetic structure with the DCS architecture (as discussed earlier), whereas, the Bi-Polar Pad (BPP) topology was chosen for the secondary. 3D Finite Element Analysis (FEA) was

Manuscript received June 30, 2016; revised September 19, 2016; accepted October 29, 2016. This work was supported in part by the government of New Zealand under Prime Minister's Science Prize 2013.

The authors are with the Department of Electrical and Computer Engineering, The University of Auckland, Auckland 1010, New Zealand (email: adeel.zaheer@auckland.ac.nz; m.neath@auckland.ac.nz; hui.beh@auckland.ac.nz; ga.covic@auckland.ac.nz)

used to design and optimize the system. In a practical situation the system components will need to be packaged appropriately before deployment; to add mechanical robustness to the system components, essential to withstand the operating conditions. This must be done in conjunction with a detailed thermal analysis to ensure that the system is equipped with suitable means for removing any excess heat generated based on installation conditions and average power demands. Note however, the work presented here focuses mainly on developing a prototype magnetic design capable of delivering the required power level, which may need further improvements to add robustness and improve thermal characteristics.

The paper starts with an overview of IPT system and the target specifications for the system presented here. After discussing the rationale behind the choice of the secondary pad and the primary track topologies, the paper describes the design refinements made to optimize the primary and secondary pads for the desired system specifications before building the prototype models for experimental validation. The material presented here, also highlights the role of the BPP topology in helping to reduce the stress on the electronic components of the system.

II. INDUCTIVE POWER TRANSFER (IPT)

IPT systems are used to transfer power from a source to the load wirelessly through electromagnetic induction. This makes the system intrinsically safe, while allowing some degree of freedom of movement to the load while it consumes power. At the heart of a typical IPT system lies a loosely coupled primary and secondary magnetic structure that is equivalent to a loosely coupled transformer. In order to deliver a significant amount of power, generally demanded by the load, despite the loosely coupled nature of the system, the primary is driven with a current source in VLF or LF frequency range (as per the SAE guidelines, 85kHz is used for EV charging applications). Therefore in medium to high power applications the primary is driven by a power supply circuit that converts the available utility power to a suitable higher frequency current source. Generally, this is accomplished by rectifying the utility power before a resonant converter is used to convert it to desired frequency and amplitude.

On the secondary side, a suitable reactive compensation network is used to improve the power transfer at the system frequency. This is followed by a power conditioning stage to meet the load requirements. Given that generally the load demands a regulated DC, therefore the output of the secondary is rectified which is then regulated using a switch mode controller before being supplied to the load. Note that the load power can also be regulated by controlling the primary current, but here the system is designed assuming that the primary is always energized at a predefined constant level (chosen to suit the overall system specifications) while any needed adjustments have to be undertaken using secondary side regulation. This also makes the system suitable to be scaled for high speed dynamic applications, where the primary might just have enough time to energize the ground pad with a

predefined fixed current level to transfer power upon detection of a fast approaching vehicle.

Although in its simplest form an IPT system can be represented by single primary inductor coupled to single secondary inductor, but depending on the nature of the application the number of the coupled primary and/or secondary inductors may be more than one. Figure 1 shows the IPT system that represents the system presented in this paper. Here, in Fig. 1(a), the primary Double-D Pad (DDP) is driven by a voltage-fed H-bridge LCL resonant converter (i.e., the output stage of the Intermediary Coupler Circuit (ICC), with the overall DCS architecture shown in Fig. 1(b), the details of which have been discussed in [27]) at a constant current I_1 at 85kHz. The secondary Bi-Polar Pad (BPP) is represented here by two inductors each separately resonated (with a parallel capacitor at the system frequency of 85kHz) and rectified before forming a common DC bus. As shown, either of the secondary coils can be decoupled, by using the two switches placed across the bottom diodes of each rectifier, if the other coil can supply sufficient power on its own [28]. The rest of the circuit forms a boost controller to regulate V_{out} .

Secondary open circuit and short circuit tests are generally quite helpful in determining the characteristics of the coupled magnetic structures in an IPT system, and then can be used to determine the rest of the system parameters. In a simple IPT system consisting of a single primary and secondary inductor, the output power of the secondary pad can be determined with the help of its secondary open circuit voltage (V_{oc}) and short circuit current (I_{sc}), and the loaded tuning factor of the secondary resonant circuit Q_2 (determined by the equivalent load across the resonated secondary due to the rectifier and the secondary switch-mode controller) as defined in (1) as [29, 30]:

$$P_{out} = |I_{sc} \cdot V_{oc}| \cdot Q_2 = S_u \cdot Q_2 \quad (1)$$

Here $V_{oc} = j\omega M I_1$ (where M is the primary to secondary mutual inductance, and I_1 is the primary current), $I_{sc} = (M/L_2)I_1$ (where L_2 is the secondary inductance) and S_u is called the uncompensated apparent power of the secondary. The output can be increased by either increasing Q_2 , the primary current (I_1), the system frequency (ω) or by improving the magnetic design (M^2/L_2). Practically, the achievable Q_2 value is limited not only by the individual unloaded component Q_s but also due to the component tolerances, imperfections and deterioration of these component values over a period of time. Similarly, I_1 and ω are also limited by the availability and cost of suitable power electronics and litz wire. Therefore, the most elegant way to increase the output is by improving the magnetic design. The S_u value is used to characterize the power transfer capability of the magnetic part of an IPT system. Whereas the constituting V_{oc} and I_{sc} values of the system can be attuned to suit the given system specifications by changing the number of turns in the secondary winding, without having any impact on the resultant S_u (assuming the Ampere-Turns injected on the primary side remain unchanged).

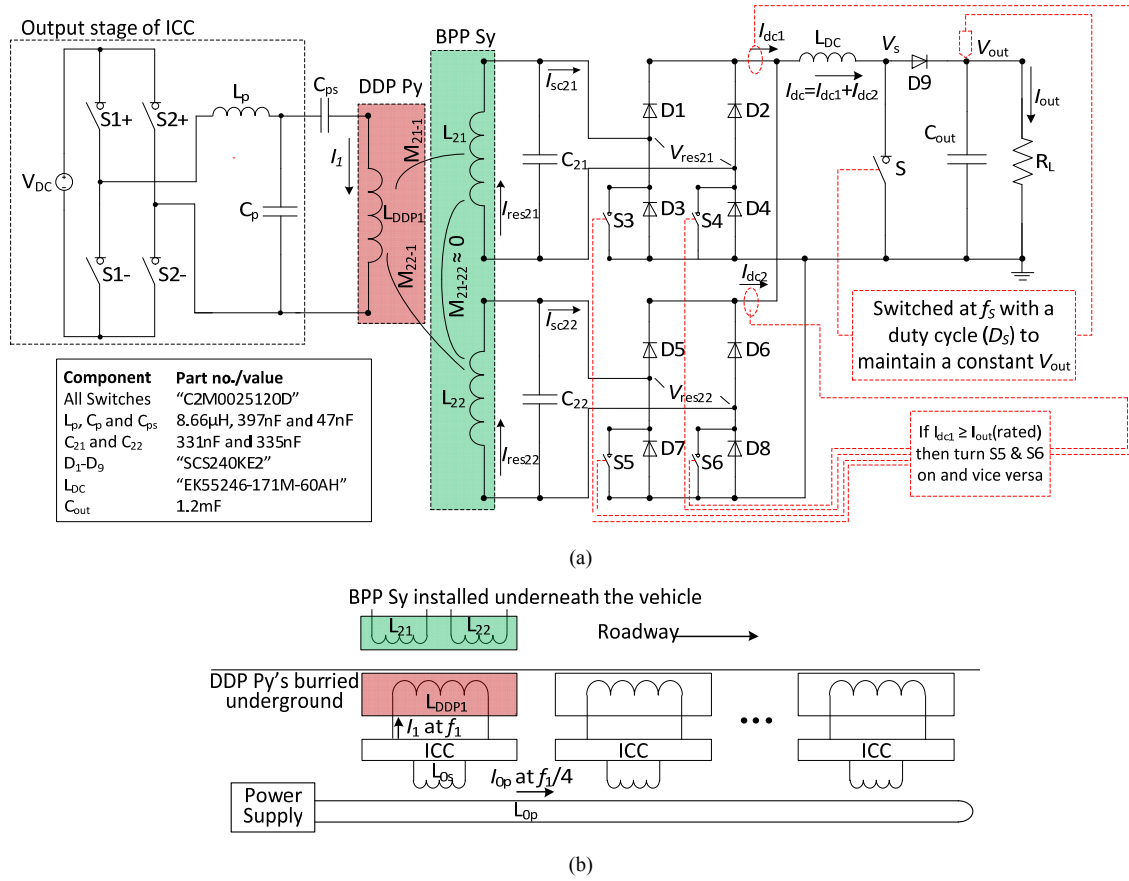


Fig. 1. (a) Circuit diagram of the IPT system consisting of an LCL tuned DDP primary, coupled to a parallel tuned BPP secondary with rectifier and boost controller (b) Simplified diagram of the Double Coupled System (DCS).

For the system shown in Fig. 1, with two mutually decoupled secondary inductors ($M_{22-21} \approx 0$; a design feature of the BPP topology [28, 31]) coupling to the same primary, this output power can be expressed as [28]:

$$P_{out} = P_{out21} + P_{out22} = S_{u21} \cdot Q_{21} + S_{u22} \cdot Q_{22} = |I_{sc21} \cdot V_{oc21}| \cdot Q_{21} + |I_{sc22} \cdot V_{oc22}| \cdot Q_{22} \quad (2)$$

Here, P_{out21} is the output power delivered to the load by the secondary inductor L_{21} with its uncompensated power represented by S_{u21} . Whereas, $V_{oc21} = j\omega M_{21-1} I_1$, $I_{sc21} = (M_{21-1}/L_{21}) I_1$ and Q_{21} are the open circuit voltage, short circuit current and operating quality/tuning factor of the secondary inductor L_{21} , respectively. Similarly the corresponding values for secondary inductor L_{22} are used here. Note that here it is assumed that a single primary pad is coupling power to the secondary coils. But in the DIPT system presented here, under certain conditions, two primary pads will couple power to the secondary coils simultaneously. In which case, the V_{oc} and I_{sc} values will represent the vector sum of the contributions made by each of the two primary pads.

The uncompensated powers and the operating Q s of the secondary remain significant for the IPT system design process, irrespective of the tuning topology used. However,

the V_{oc} and I_{sc} values can have additional significance, depending on the used secondary tuning topology. A parallel tuned secondary, used in the system presented here, behaves like a current source for the load and is generally preferred because of this inherent current limiting property. This means that from the perspective of the equivalent load connected across a parallel tuned secondary; only the voltage is boosted by the operating quality factors (i.e., $V_{res21} = V_{oc21} \cdot Q_{21}$ and $V_{res22} = V_{oc22} \cdot Q_{22}$) whereas the current provided to the load remains limited to the total of the secondary short circuit currents.

Assuming that the V_{out} is maintained at its rated value by the control action with all components being ideal (this also implies ideal tuning) and L_{DC} is large enough to keep the rectifiers in continuous conduction mode with I_{dc} as an ideal ripple free DC current [32, 33]:

$$I_{dc} = I_{dc1} + I_{dc2} = (|I_{sc21}| + |I_{sc22}|) \cdot \pi / 2\sqrt{2} \quad (3)$$

In this way the output power for such a system can also be represented as:

$$P_{out} = I_{out} \cdot V_{out} = I_{dc} (1 - D_s) \cdot V_{out} \quad (4)$$

For the battery charging applications V_{out} (voltage across

the battery terminals) will be more or less constant at its rated value, under the normal circumstances. This shows that the rated P_{out} can only be maintained using the control action (provided by varying D_s between 0 through 1) when $I_{dc} \geq I_{out(rated)}$. Therefore, Equation (4) in combination with Equation (3) shows that in order to deliver the rated P_{out} to the load, the secondary must be designed to ensure total short circuit current $I_{sc} = (|I_{sc21}| + |I_{sc22}|) \geq I_{out(rated)} \cdot 2\sqrt{2}/\pi$. This highlights the significance of the secondary short circuit current in such a system.

Furthermore, for instance, if under certain operating conditions $|I_{sc21}| \geq I_{out(rated)} \cdot 2\sqrt{2}/\pi$, then the rated power can be delivered without any contribution from the other coil L_{22} . Therefore, due to the mutually decoupled nature of the secondary coils ($M_{22-21} \approx 0$), it is possible to turn S5 and S6 on to make $I_{dc} = I_{dc1}$ (and make the necessary adjustment to D_s) to improve the efficiency and lower the ratings of the components. Similarly S3 and S4 may be turned on if $|I_{sc22}| \geq I_{out(rated)} \cdot 2\sqrt{2}/\pi$ [28].

Electric vehicles are divided into various classes based on their power ratings and ground clearances; here the objective of this study was to build a practical system that could provide a good launching pad for further exploration and improvements. As mentioned earlier, the system in this paper is designed to suit slow moving in road applications where it is desired to transfer full rated power continuously along the whole length in the direction of travel with some tolerance to lateral misalignment. As per SAE guidelines, the system was designed to operate at 85kHz and the rated output power P_{out} was chosen to be 15kW. The desired tolerance to lateral misalignment, while delivering the full rated power, was chosen to be ± 200 mm. The system was designed for a primary to secondary coil to coil distance of up to 200mm in this study. This was chosen based on the typical ground clearance for a small or compact car designed to be used primarily in the urban areas, where the primary is flush mounted at ground level.

III. CHOICE OF PRIMARY AND SECONDARY MAGNETIC TOPOLOGIES

As explained in [34], lumped magnetic pad designs can be categorized into parallel flux only, perpendicular flux only and hybrid flux designs. The parallel flux only pad designs (i.e., the DDP and solenoid type pads) have been shown to have the ability to couple power over larger air gaps as compared to the perpendicular flux only pad designs (i.e., the Circular Pad (CP)) [26]. Whereas, the hybrid flux pad designs consisting of mutually decoupled multi coil structures (i.e., the Double-D Quadrature Pad (DDQP) and the BPP) have an obvious performance advantage over both the parallel flux only and the perpendicular flux only pad designs, when tolerance to relative misalignment is essential. This is because of their ability to generate both parallel and perpendicular flux patterns on demand when used as primaries (as discussed in [34]) and their ability to couple both parallel and perpendicular components of flux when used as secondaries (as discussed in

[35]). But this improvement in performance comes at the cost of an increase in the complexity of both the magnetic and electronic design on the side of the system (primary/secondary) that uses the hybrid flux pad.

Generally, parallel flux only and hybrid flux pad topologies are polarized to couple flux only along one of the two dimensions (either the length or the width) of the pad. Therefore, the pads can be oriented to either align the direction of polarization with the direction of travel or perpendicular to this direction (as discussed in [36, 37]), although some angle between these two options may also be possible. In any of these cases, for an effective operation, the direction of polarization of the secondary should also align with that of the primary pads. The orientation where the polarization of flux is perpendicular to the direction of travel has been discussed in [36]. The scope of this study is limited to the pad orientation where the direction of polarization is aligned with the direction of travel (as shown in Fig. 2) given this is the orientation chosen for similar polarized topologies for buses and rail [16, 20, 21, 38, 39], and is the preferred orientation at present in stationary charging applications [40].

Various combinations of primary and secondary pad topologies for the chosen orientation of flux polarization have been discussed in [37]. The system presented in this paper uses the DDP topology for the primary pads and the hybrid flux BPP as the secondary pad topology. The rationale behind these choices is explained following.

The nature of the DIPT system discussed here means that the operation of the adjacent primary pads has to be synchronized at some level to ensure continuous power transfer to the secondary load on the move. This naturally increases the complexity of the primary side design. While using a more complex primary pad design (using 2-phase or 3-phase multicoil structures) provides certain performance benefits [37], this complicates and increases the cost of the primary design due to the number of tuned coils per meter and associated power supplies. Therefore, it was decided to use a simple single winding primary pad topology. This focused the choice between DDP and CP (or Rectangular Pad (RP)) topologies to form the primary track. The discussion presented in this paper covers only the first of these two options.

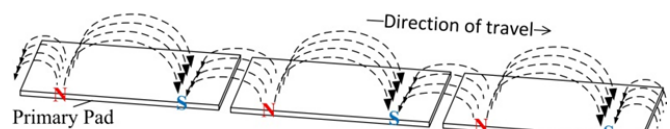


Fig. 2. Parallel flux patterns generated by the primary pads; polarized along the direction of travel.

With such a primary side layout, it is impossible to ensure a continuous transfer of power to any single winding secondary pad (whether DDP or Circular/rectangular). This is because even when the secondary is laterally aligned with the primary track layout, it will encounter significant regions along the direction of travel where only the parallel or perpendicular flux components are strong enough to link to the secondary and allow power transfer. Thus these simple secondary pads will experience null power points along the direction of travel.

The usage of a hybrid flux secondary pad topology, on the other hand, provides a continuous power transfer without any null power points along the direction of travel. While both the BPP and the DDQP are suitable, the BPP uses less material with similar performance [35] and was chosen for this study.

The pads forming a primary track can be energized either in-phase or out of phase w.r.t. the adjacent pads. As shown in [37], in case of a primary track formed by the DDPs; the in-phase operation allows larger gaps between the adjacent primary pads, when used with a BPP secondary. As their primary to secondary power transfer profiles do not deteriorate severely with increasing gaps. Although this primary and secondary topology combination does show significant variation in power transfer (i.e., around 70% variation within the region of interest), but as explained earlier in section II, the ability to turn one of the secondary BPP coils off when needed, can help reduce these power variations as the vehicle moves along the track.

IV. PRELIMINARY MODELS FOR THE PRIMARY AND SECONDARY PADS

This section provides the constructional details of the preliminary models for the DDPs used to form the primary track and the BPP secondary. As a starting point for the study, the primary and secondary pad designs were chosen to match the designs used in [37], which were refined throughout the length of the optimization study, presented here, to meet the design goals. However, unlike the BPP primary pads (operated in DD-mode) used in [37], here the primary track is formed using the DDPs. Therefore, the DDP design used in [34] was used for the primary pads. This is because in [34] this DDP design has already been shown to generate almost identical results as that generated by the primary BPP design used in [37] when the two coils are operated with the currents that are out of phase (i.e., DD-mode).

Given that the volume and weight of the secondary pad design is generally more constrained than the primary side, the overall size of the secondary pad was fixed for this study (i.e., the size used for the study presented in [37]) while the rest of the parameters could be attuned accordingly to achieve the desired performance. As explained in [37], the length of the secondary pad was chosen to almost match the pole width of the primary pad (i.e., 700mm), however, the width of the secondary pad was limited to 350mm to constrain the coupled S_u and allow some tolerance to lateral movement. Figure 3 shows the construction of the DDP primary and the BPP secondary pads, with the preliminary values of various design parameters given in Table I.

The secondary pad (used in [37] and in turn here) was designed to be able to couple as much flux as possible (by possibly taking excessive design measures) while keeping the overall pad size within predefined limits. In the secondary pad, five ferrite strips were used as compared to the four strips used in the primary. The extra ferrite strip, used here, can help lower the reluctance of the flux path. In addition, as highlighted both in Fig. 3 (b) and Table I, the width and thickness of the horizontal and vertical arms of the coils in the

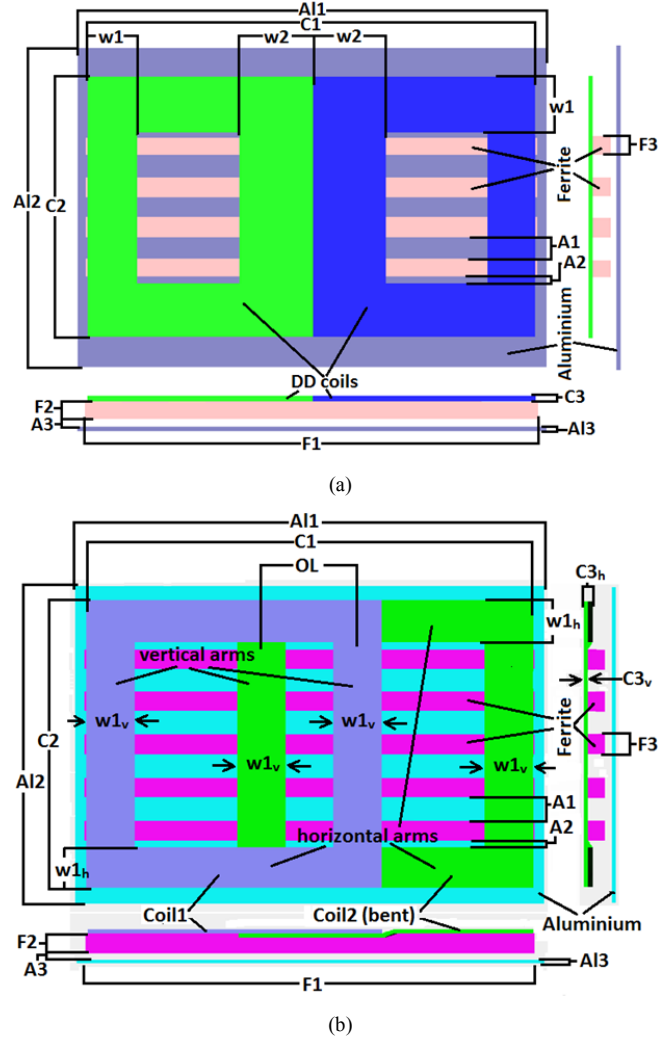


Fig. 3. Construction of the pads (top and side views) with dimension labels (a) DDP (b) BPP.

TABLE I
PRELIMINARY VALUES OF DESIGN PARAMETERS

Design Parameters	BPP Sy	DDP Py
Number of ferrite strips	5	4
A11 (mm)	700	775
A12 (mm)	350	485
A13 (mm)	4	4
A1 (mm)	25	33
A2 (mm)	5	10
A3 (mm)	6	6
C1 (mm)	680	738
C2 (mm)	330	391
C3v (mm)	4	4
C3h (mm)	8	4
F1 (mm)	680	744
F2 (mm)	16	16
F3 (mm)	28	28
w1v (mm)	80	80
w1h (mm)	40	80
w2 (mm)	--	120
OL (mm)	140.5	--

secondary (represented by $w1_h$, $w1_v$ and $C3_h$, $C3_v$) are also different, as the horizontal arms are wound in two layers compared to single layer winding of the vertical arms. This

winding structure helps couple more flux given that it results in a larger mean area of the secondary coils, directly facing the flux generating area of the primary pads.

All the parameters of Table I were chosen to enable the primary and secondary pads to be built using available 6.36mm² litz wire (consisting of 810 strands of AWG 38 wire and having an overall diameter of ≈ 4 mm) and blocks of N87 ferrite material (each 93mm \times 28mm \times 16mm). This litz wire is rated for 23A and all the initial designs began by assuming unifilar windings with each coil having 20 turns.

V. MAGNETIC DESIGN REFINEMENTS FOR THE CHOSEN ARRANGEMENT

The simulation setup used here is similar to that described in [37]. The primary side consisted of 4 DDPs, with the two middle pads (DDP2 and 3) energized in-phase w.r.t. each other. The secondary pad was placed at a coil to coil distance of 200mm from the primary and coupling was evaluated as it was moved along the direction of travel, as shown in Fig. 4. As shown, the direction of travel is along x-axis, whereas the lateral displacement is along y-axis. Both x and y-displacements are defined to be 0mm when the secondary pad is aligned with the centre point of the primary track formed by the 4 DDPs. The system is symmetric in both x and y-directions across this central point. The two extremes across which the secondary is swept in x-direction are also highlighted in the figure, with negative extreme representing the position when secondary is aligned with DDP1 and

positive extreme when it is aligned with DDP4.

Based on the results presented in [37] the gap between adjacent primary pads was chosen to be 200mm (the largest value considered in [37]). The simulation setup shown in Fig. 4 remains unchanged throughout this paper, while the designs of the constituting pads are refined to meet the target system specifications. The uncompensated powers and the magnitudes of the short circuit currents for each secondary coil (S_{u21} , S_{u22} and $|I_{sc21}|$, $|I_{sc22}|$) along with their respective sum totals ($S_u = S_{u21} + S_{u22}$ and $I_{sc} = |I_{sc21}| + |I_{sc22}|$), for the system setup shown in Fig. 4, where the primary and secondary pads are built using the preliminary designs presented in Table I, are shown in Fig. 5. Here the middle point of each of the four primary DDPs is also highlighted for clarity.

As described in section II, in order to achieve the rated P_{out} of the system, the magnetics have to be designed to have a secondary short circuit current $I_{sc} \geq I_{out} \cdot 2\sqrt{2}/\pi$. Under the assumption a car battery voltage is between 350-450Vdc, a system designed to deliver $P_{out} = 15$ kW at $V_{out} = 450$ Vdc requires $I_{out} = 33.3$ A. Thus, the minimum value of I_{sc} required is around 30 A. Notably this is much higher than the values attained using the preliminary simulations (Fig. 5), but this can be easily fixed by rearranging the secondary winding to have fewer turns (while using enough copper to accommodate the expected current magnitudes), as long as, the secondary operating Q s required to turn on the diodes in their respective rectifier circuits do not become unrealistically high for a practical system.

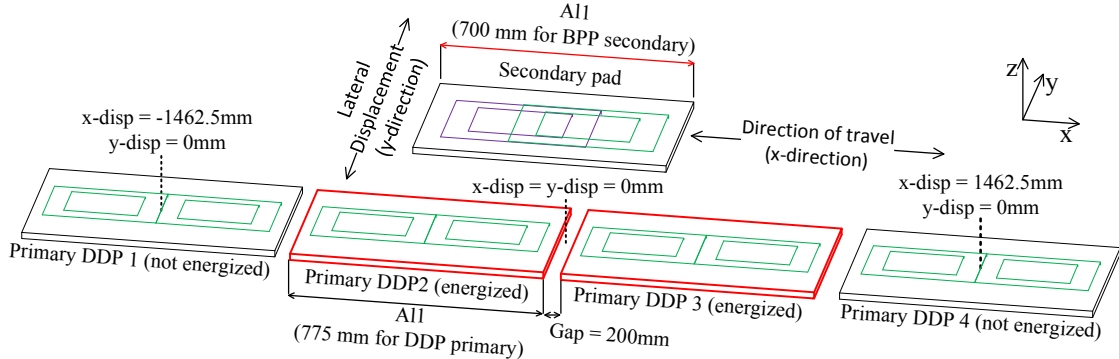


Fig. 4. Simulation setup – Four primary pads (DDPs) with the two middle ones energized and a secondary pad (BPP) swept along the direction of travel

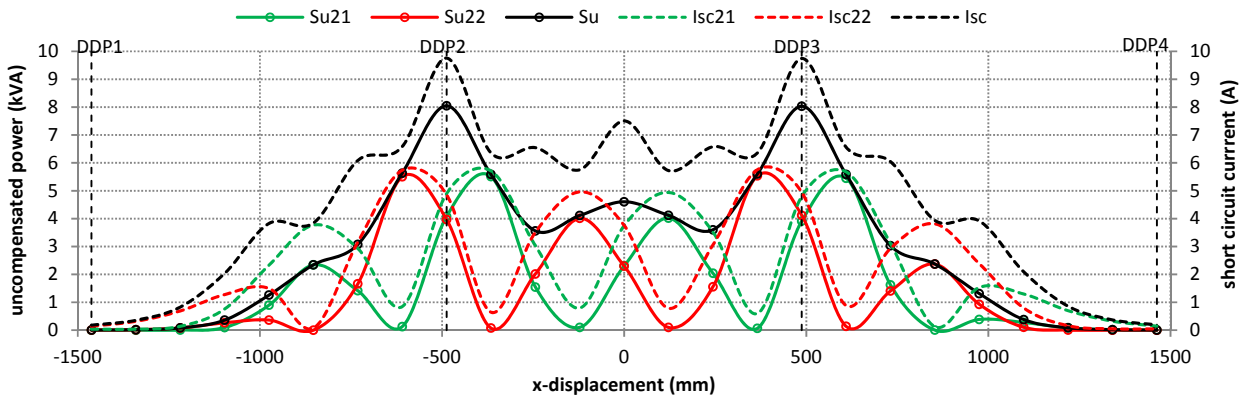


Fig. 5. The magnitude of secondary short circuit currents and uncompensated powers as a function of x-displacement of the secondary pad (with y-displacement=0mm) for the selected primary side arrangement; using the preliminary designs for the primary DDPs and secondary BPP

The systems having high component Q s (i.e., Q_{L21} , Q_{C21} and Q_{L22} , Q_{C22} ; representing the inherent resistive losses in individual components forming the resonant circuits) can achieve reasonably high values of the operating Q s (i.e., Q_{21} and Q_{22} ; representing the sharpness of the circuit resonance). But given that the efficiency decreases with increasing operating Q s, it is desirable to keep these Q s below a reasonable limit, even if higher values may be achievable. Therefore, generally, the S_u values are used to assess the power transfer capability of the system, while staying within the desired limit for the secondary operating Q s (generally under 10, as at this point the magnitude of resonant current circulating within the resonant circuit is around 10 times higher than its current contribution towards the load). Whereas, the decision on the primary and secondary winding arrangements (number of turns and current carrying capacity), is left till the later part of design process.

As demonstrated in [28, 31], an approximate rule of thumb can be used to simplify the magnetic design criteria when dealing with the multicoil pads, to facilitate a quick assessment during the magnetic optimization process. As per this approach the multicoil secondary can be assumed to consist of a single winding structure, with a single cumulative operating quality factor Q_2 ; while further restricting its desired value to under 5 (which provides a suitable safety margin for the individual operating Q s that are ideally desired to remain under 10) and $P_{out} \approx (S_{u21} + S_{u22}) \cdot Q_2 = S_u \cdot Q_2$. This approach works due to the inherent characteristics of the multicoil hybrid flux designs (i.e., BPP and DDQP); because one constituent coil couples increasingly large amount of power as the power coupled by the other reduces due to a change in primary to secondary misalignment. Consequently, by the time the power coupled by one coil reaches such a low level to require an operating Q double the assumed cumulative Q , generally, the other coil is already coupling enough power to drive the load on its own at a much lower operating Q .

When these S_u values are analysed based on the above mentioned approximation, it seems that the required P_{out} of 15kW can be easily achieved with a Q_2 of around 5 between the x-displacement range of about ± 750 mm (with DDP2 and 3 energized in-phase). This means that by suitable selection of secondary turns ratio this preliminary magnetic design can achieve continuous power transfer along the direction of travel when the BPP secondary is laterally aligned with the primary track (i.e., y-displacement=0mm). Because, for instance, if the secondary is moving from DDP3 towards DDP4, it gives the system an x-displacement range of around 250mm (i.e., from 490 to 750 mm) to detect the secondary's movement towards DDP4. Once this movement is detected, in order to ensure the continuous transfer of rated power, DDP2 can be de-energized and DDP4 can be energized (in phase with DDP3) to create a similar S_u -profile between DDP3 and 4 that exists between DDP2 and 3 in Fig.5. This also reduces the region of interest to the x-displacement range between ± 750 mm, which can be further narrowed down to any one half around its centre point by exploiting the symmetry of the system around x-

displacement=y-displacement=0mm. However in order to achieve a system that can tolerate a lateral/y-misalignment of ± 200 mm while delivering a P_{out} of 15kW, these preliminary pad designs will need further modifications. These modifications are discussed following.

A. Secondary Pad Design Refinement

Before reporting the outcomes of the secondary BPP design refinement process, it is important to emphasize that any change in any dimensional parameter of a BPP; can potentially change the resulting flux paths generated by the BPP coils and consequently requires readjustment of the overlap (OL) between the two BPP coils in order to maintain the mutually decoupled status of the two coils [31, 35].

After various iterations it was found that increasing the spread of the vertical arms (w_{lv}) of the BPP coils from 80mm to 120mm (by introducing uniform gaps between adjacent turns in these sections of the coils) results in a reasonable reduction in the overall variation in S_u -profile, as the secondary is displaced within the relevant x-displacement range of ± 750 mm (a reduction of around 1kVA in the gap between maximum and minimum power levels, as compared to the original design of Table I). Any such reduction is desirable as it reduces the cost (by allowing the use of relatively low component ratings) and increases the efficiency of the secondary regulator circuit. Note that all the other design parameters of the original design (given in Table I) were kept constant to observe only the impact of varying the value of w_{lv} , with the only exception being the readjustment in OL. The value of OL required to maintain the mutual decoupling between the two BPP coils having $w_{lv}=120$ mm was found to be 121.5mm.

Further increments in the value of w_{lv} were not considered as it would have required increasing the overall thickness of the secondary pad, unless the thickness of the ferrite structure was to be reduced in the middle region of the secondary pad. But such a reduction was deemed undesirable as it could result in saturating the resulting thinner ferrite region; in case of out of phase current flows in the BPP coils [28].

Furthermore, it was found that the usage of an extra ferrite strip (i.e., 5 instead of 4 strips used in the similar sized pads [26, 34, 35], as well as in the primary DDPs used here) only results in an increase of around 2% in the amount of power transferred to the secondary (regardless of the misalignment) when compared with a secondary having only 4 ferrite strips. This increase was deemed insufficient to justify a 25% increase in the ferrite material used to build the secondary pad and hence a 4 ferrite strip secondary was chosen as the preferred option. Note that the spacing between the adjacent ferrite strips for this 4 strip secondary model was matched with the primary DDPs i.e., $A1=33$ mm, while $A2$ was 19.5mm and readjusted OL=144mm, with the rest of the parameters kept as reported in Table I. However further decreases in ferrite were also investigated but resulted in a sharper decrease in power transfer, more importantly it was found to be insufficient to keep the ferrite in the linear region of its BH-curve under the worst case loaded operating conditions of the

system.

B. Primary Pad Modification

As shown in Fig. 6(b), laterally displacing the secondary pad (i.e., in y-direction) by 200mm from the centre of the track results in the S_u value reducing to $1/3^{\text{rd}}$, for the original system constructed using the pad designs given in Table I. The resulting value at this displacement requires a cumulative operating quality factor (Q_2) of around 10, which is much higher than desirable.

Notice that the S_u reduction is around 25% for an increase in y-displacement from 0 to 100mm and for a further increase to 200mm it reduces at a faster rate further halving the S_u value. This effect is due to the difference in the widths of the primary DDP relative to the secondary BPP (i.e., 485mm for DDP compared to 350mm for the BPP). For the larger values of y-displacement (i.e., greater than $((485\text{mm}-350\text{mm})/2) = 67.5\text{mm}$) the slope becomes steeper, because the area of the secondary pad (coupling the flux) directly facing the primary pad (generating the flux) increasingly becomes smaller and smaller. Therefore the rate of reduction in the S_u -profile can be improved by increasing the width of the DDP primaries. A downside to making this change is that it will also raise the overall S_u -profile.

The results for the system where the width of the primary DDPs (A11) is increased from 485mm to 600mm (while C2 is likewise increased from 391mm to 574mm) are also shown in Fig. 6 for comparison. The number of ferrite strips used in the primary DDPs was also increased from 4 to 7, but the rest of the design parameters (primary DDP and secondary BPP) were kept the same as in the preliminary designs of Table I.

As shown in Fig. 6(a), the increased width of the primary DDPs, increases the whole S_u -profile by almost 60%. More importantly, Fig. 6(b) shows that the S_u value only drops to a half for a lateral displacement of 200mm compared with a $1/3^{\text{rd}}$ in the preliminary design. This lowers the required value of Q_2 to around 4 at this extreme lateral displacement, which is within the desired limit.

It is worth noting here that the y-displacement plot shown in Fig. 6(b) doesn't show the worst case scenario. As if the y-displacement power profile is plotted for x-displacement $\approx \pm 240\text{mm}$ (i.e., the two minimas located on each side of the middle point of the primary track, one of which is

visible in Fig. 6(a)), will result in a lower overall profile than the one shown in Fig. 6(b). Given that such a profile will exhibit almost identical rate of reduction (i.e., halving the amount of power when misaligned by 200mm in y-direction), the worst case Q_2 value expected is between 5 and 6.

Notably, as shown in Fig. 6(a), a spike in power transfer occurs as the secondary aligns with one of the energized primary pads (in this case with DDP3 at x-displacement=487.5mm). But here the ability of the BPP secondary to decouple or turn off one of the coils, when the other coil couples sufficient power to support the load on its own, can be utilized to dampen these abrupt variations in power. This option is discussed further in section VII.

VI. PAD DESIGNS FOR THE PROTOTYPE MODELS

Based on the results of the design iterations presented in the last section, new primary and secondary design parameters were chosen for the prototype system, with parameters detailed in Table II. The decisions that helped determine the winding arrangements are discussed below. Of primary concern was to ensure that it was suitable for the primary electronics to energize the DDPs (i.e., the ratings of the switches forming the H-bridge and the capacitors used for primary resonance etc.), while the BPP could handle the resonant current levels expected while delivering the power at the chosen V_{out} and I_{out} levels to the load. In addition, the ease of winding and the availability of the litz wire were also the factors considered when making these decisions.

A 12.72mm^2 litz wire (consisting of 1620 strands of AWG 38 wire and rated for 50A current) was chosen to wind the primary DDPs (instead of the 6.36mm^2 litz wire). This means that the thickness of the winding (C3) is increased to 6.6mm from 4mm. The winding was bifilar wound with 6 turns, and energized at its maximum rated current of 100A at 85kHz. Note that the resultant extra copper, packed in the primary DDP, allows additional Ampere-Turns to be pumped into the pad (600 AT compared to 460 AT). This heightens the resultant S_u -profile further, and enables a secondary pad to extract larger amount of power from the primary side, providing it is rated to handle that power. Whereas, each of the secondary BPP coils was wound using 6.36mm^2 litz wire but configured as a penta-filar winding with 4 turns.

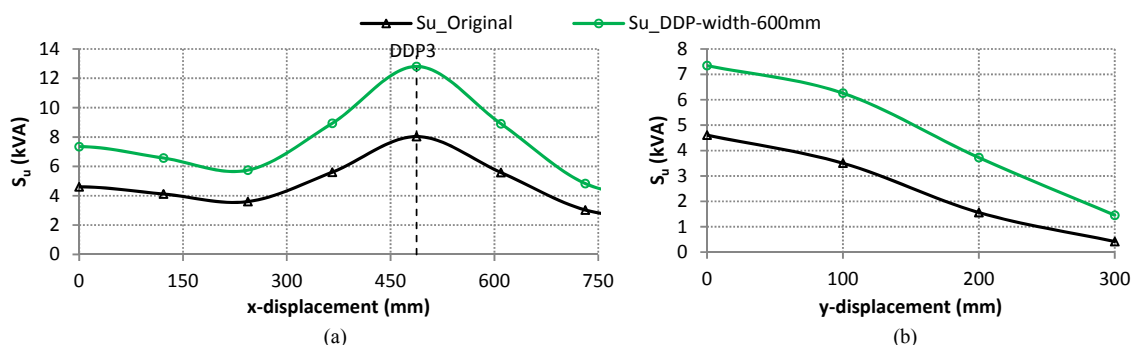


Fig. 6. Total uncompensated output power ($S_u = S_{u21} + S_{u22}$); for the system using preliminary and the modified design for the DDPs, when displaced (a) in x-direction with y-displacement=0mm and (b) in y-direction with x displacement = 0mm

TABLE II
DESIGN PARAMETERS FOR THE PROTOTYPE MODEL

Design Parameters	BPP Sy	DDP Py
Number of ferrite strips	4	7
A11 (mm)	700	775
A12 (mm)	350	600
A13 (mm)	4	4
A1 (mm)	33	33
A2 (mm)	19.5	10
A3 (mm)	6	6
C1 (mm)	680	738
C2 (mm)	330	574
C3 _v (mm)	4	6.6
C3 _h (mm)	8	6.6
F1 (mm)	680	744
F2 (mm)	16	16
F3 (mm)	28	28
w1 _v (mm)	120	80
w1 _h (mm)	40	80
w2 (mm)	--	120
OL (mm)	129	--

The resulting simulated I_{sc} and S_u -profiles are presented in Fig.7. Here the secondary BPP is swept through the x-direction five times, each time with a different value of y-displacement.

These results show that the system is capable of delivering the required power of 15kW, with a lateral (y-direction) displacement of up to 200 mm. As, the minimum S_u value, between any two adjacently placed energized primary DDPs, remains above 5kVA with the minimum I_{sc} value of about 35A. Both these values meet the requirements defined in section V. Note that the design provides a 5A margin, beyond the required value of 30A. This margin is meant to help ensure that when one coil's power contribution towards the load is reduced to just around 10% of the total due to a change in misalignment and it is reaching an undesirably high operating Q , the other coil might be able to drive the load on its own using a much lower operating Q .

Furthermore, the simulated results also show that the overall variation (covering the defined operational primary to secondary misalignment region) in the self-inductance of each BPP coil ($L_{21} = 11.04$ to $11.28 \mu H$ and $L_{22} = 11.07$ to $11.28 \mu H$) is less than $\pm 1.5\%$ with the maximum coupling between the two BPP coils ($k_{21-22} = 3.7$ to 5.4%) reaching 5.4%. Both these values are small

enough for the two coils to be independently tuned and operated.

The results also show that the maximum variation in the self-inductance of a primary pad ($L_{DDP_1} \cong 81.7$ to $85.3 \mu H$) occurs when the secondary pad is centrally aligned with it, in which case its self-inductance is increased by around 4.3%. The maximum coupling (around 1.8%) between two adjacent pads occurs when the secondary pad is positioned right in the middle of these two pads, with the overall range of variation being $k_{DDP_n-DDP_{n+1}} \cong 0.56$ to 1.77% . Again these values show that the variation in the inductance values is minimal, which means that these pads can be easily driven by a resonant power supply and the power coupled from an energized pad to an adjacent non-energized pad is also insignificant.

VII. OPERATIONAL DETAILS AND FEATURES

Figure 8 shows the S_u and I_{sc} values for each BPP coil, when the secondary BPP is laterally aligned with the primary track (i.e., zero y-displacement) under two different conditions. First, when only one primary pad (DDP3) is energized while in the second case, two adjacent primary pads (DDP2 and DDP3) are energized. This highlights that depending on the position of the secondary BPP with respect to the track, the system can be controlled and operated in different ways to deliver the rated power efficiently.

For instance, between the points A and B the required rated power of 15kW can be delivered to the load by energizing only one primary pad (DDP3), thereby avoiding the losses that will occur by energizing DDP2 as well. Furthermore, within the x-displacement range between points C and D, one of the two BPP coils may also be turned off (i.e., short circuited using S3-S6) while the other supports the load on its own. This helps dampen the spike in power that occurs between these two points, reducing the stress on the components connected between the output of the secondary rectifiers and the load. Consequently, the maximum design value of I_{dc} for these components reduces from 90A to around 55A. Turning one of the secondary BPP coils off, where possible, has also been shown to reduce the losses and improve overall system efficiency in [28], however the work presented in this paper is limited to highlighting the reduced stress on the secondary components.

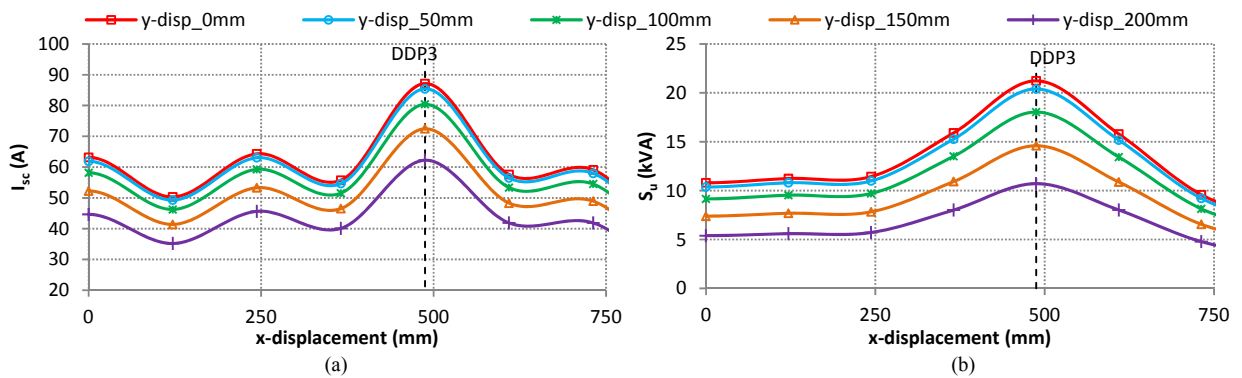


Fig. 7. (a) I_{sc} (i.e., $|I_{sc21}| + |I_{sc22}|$) and (b) S_u (i.e., $S_{u21} + S_{u22}$) for the prototype pad designs; here the secondary pad is swept through the x-direction with fixed y-direction displacements of 0, 50, 100, 150 and 200mm

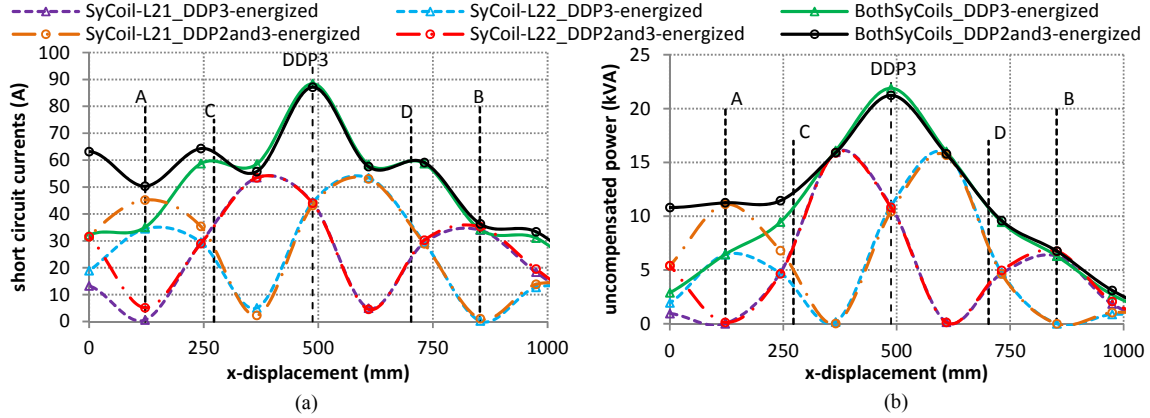


Fig. 8. (a) Secondary short circuit current magnitudes and (b) Uncompensated output power for the prototype pad designs; here the secondary pad is swept through the x-direction with y-displacement=0mm

This discussion highlights the significance of detecting the position of the secondary pad, as well as, monitoring the amount of current delivered by individual secondary BPP coils to the load. The details of the detection and primary side control mechanism are beyond the scope of this publication but are discussed in [41].

As discussed in section II, under the assumption of ideal components and tuning there is no limit on the operating Q s of the secondary coils and the power delivered to the load after regulation by the secondary boost controller is given by (4). However if it is assumed that the switch S is permanently open circuited i.e., $D_s = 0$, the secondary boost controller will behave as a simple low pass filter and all the power available at the input of the controller ($P_{out_available} = I_{dc}V_{out} = P_{out}/(1 - D_s)$) will be delivered to the load without regulation. The variation in the value of this $P_{out_available}$ should, ideally, be minimum to reduce the ratings of the components used in the regulator circuit. The case, where the decoupling switches S3-S6 are not used (i.e., permanently open circuited) and both coils are employed to deliver power to the load irrespective of the position of the secondary relative to the primary track, is referred here as “Ctrl1” operation. Under Ctrl1 operation, the plots showing the $P_{out_available}$ will be identical in shape to the I_{sc} -plots shown in Fig. 7(a) (see Eq. (3) and (4)) with rapid peaks in power occurring when the secondary pad aligns with one of the energized primary pads (DDP2 and 3 in this case). This results in a ratio of almost 2.5 between the minimum and maximum coupling power points within crucial x-displacement range of ± 500 mm. The plots shown in Fig. 9, highlight that how this maximum to minimum variation ratio in coupled power can be reduced to around 1.8 by using decoupling switches S3-S6 to selectively isolate one of the secondary coils, referred here as “Ctrl2” operation. Figure 9(a), shows the $P_{out_available}$ values as a function of x-displacement with various lateral offsets, under Ctrl2. Figure 9(b) further highlights this variation reduction process by comparing the plots with (Ctrl2) and without the usage of decoupling switches (Ctrl1) for the lateral/y-displacement of 200mm.

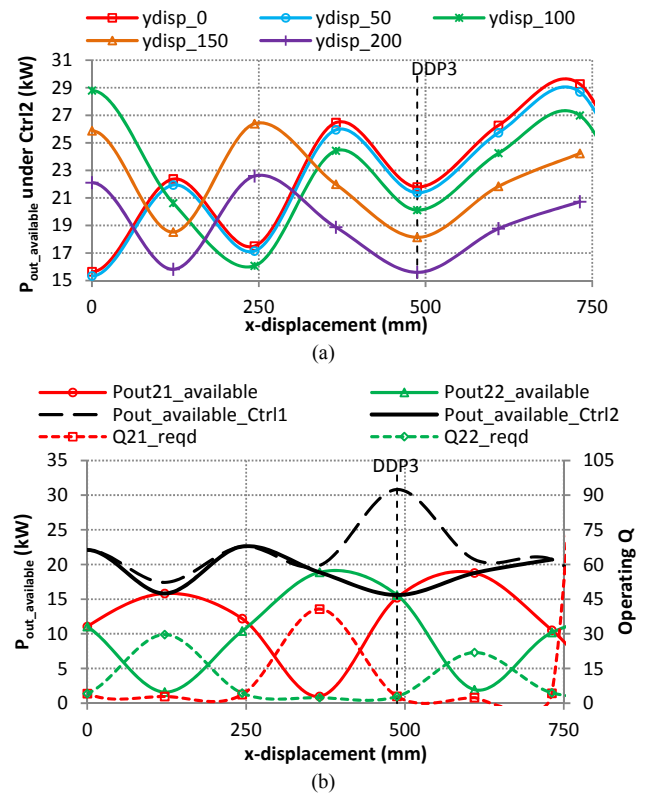


Fig. 9. $P_{out_available}$ as a function of x-displacement (a) under Ctrl2 operation for various lateral displacements and (b) comparison of Ctrl1 and Ctrl2 operation for lateral displacement of 200mm along with corresponding operating Q values of individual secondary coils

VIII. EXPERIMENTAL VERIFICATION

The prototype models were built using the pad design parameters given in Table II, to experimentally verify the simulated results. All the experimental measurements were conducted for a coil to coil distance of 240mm instead of 200mm, due to the height of the available platform used to conduct the experiments. Therefore, in order to validate the accuracy of the simulations, the system was re-simulated for a coil to coil distance of 240mm and then compared with the experimental results.

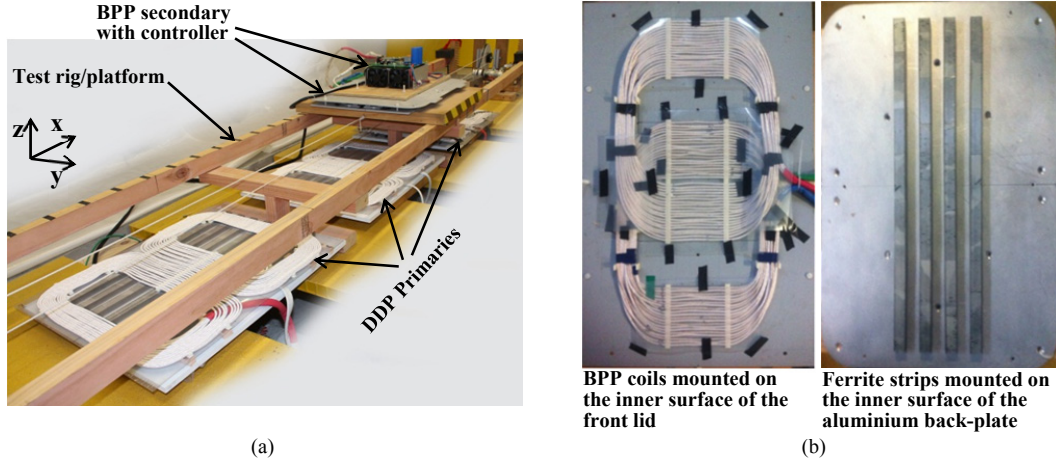


Fig. 10. Photograph of the prototype system used for experimental verification (a) primary track and secondary pad with controller (b) the construction of the secondary BPP

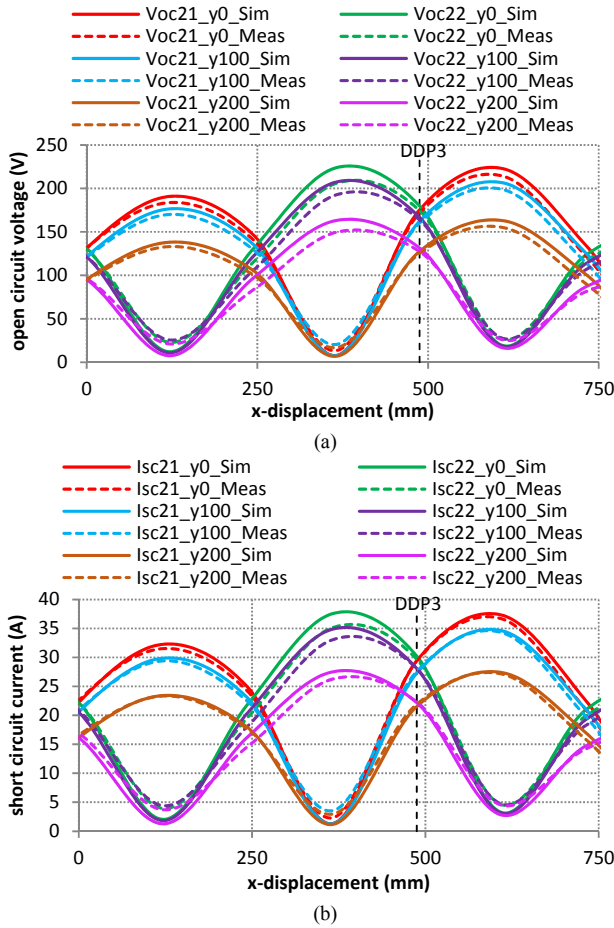


Fig. 11. Comparison between the simulated and measured values of the (a) Secondary open circuit voltage and (b) short circuit current magnitudes

Figure 10 shows a picture of the prototype system, with the results of open and short circuit secondary tests shown in Fig. 11; along with the simulated results for comparison. The construction of the prototype of the secondary BPP is also shown here in Fig. 10(b).

Figure 11 shows the open circuit voltages and short circuit currents for individual secondary BPP coils, as it is swept along the x-direction, for each of the y-displacements of 0,

100 and 200mm. These results are presented for the case when both DDP2 and DDP3 are energized in phase with a current of 100A at 85kHz. As shown, the simulated and measured values are in good agreement and verify the ability of the pads to deliver the voltage and current levels required to drive the load. Note however that these results were calculated using the formulae for V_{oc} and I_{sc} values given in section II; after measuring the relevant self and mutual-inductance values of the pads as a function of primary to secondary x and y-displacements assuming $I_1 = 100A$ and $\omega = 2\pi(85000) \text{ rad/sec}$.

Figure 12(a) shows the simulated and measured values of inductances of each of the BPP coils (L_{21} and L_{22}), as the secondary is swept along the x-direction (with y-displacement=0mm). In order to validate the effective mutual decoupling of the two BPP coils; the impact of shorting one of these coils (BPP coil1 (L_{21}) in this case) on the inductance of the other coil (BPP coil2 (L_{22})) is also shown here. As expected the simulated and measured results are in good agreement and show that for a primary to secondary coil distance of 240mm, the variation in inductance is further reduced to be less than 1% (as compared to $\pm 1.5\%$ for the distance of 200mm, as reported in section VI), and the two BPP coils are effectively mutually decoupled as the impact of the primary pads on their inductance is quite minimal.

Similarly, in order to assess the mutual coupling between the adjacent primary DDPs (DDP2 and DDP3), their in phase ($L_{DDP2} + L_{DDP3} + 2M_{DDP2-3}$) and out of phase inductance ($L_{DDP2} + L_{DDP3} - 2M_{DDP2-3}$) values were measured w.r.t. the position of the secondary pad as it is swept in x-direction (with y-displacement=0mm). These two values were then used to separate the value of the mutual inductance between DDP2 and DDP3 (M_{DDP2-3}) and the sum of their self-inductances ($L_{DDP2} + L_{DDP3}$). All of these four values, along with the corresponding simulated values are shown in Fig. 12(b) as a function of secondary pad's x-displacement.

The variation in the self-inductance of the individual DDPs due to the secondary pad is also reduced further due to the increase in primary to secondary coil to coil distance and is

now just around half a per cent. The coupling between adjacent primary pads DDP2 and DDP3 has also shown a marginal reduction (with the peak coupling co-efficient k_{DDP2-3} being around 1.5%). These results verify the predictions made on the basis of the simulated results presented in section VI.

All the inductance measurements, presented here, were performed using Agilent's E4980A Precision LCR Meter. Note that only the x-direction sweeps for y-displacement=0mm are shown here in Fig. 12, to save space, as the variation in inductance is maximum when the pads are laterally aligned.

The ability of the system to turn one of the secondary BPP coils off, under suitable conditions (i.e., Ctrl2; as described in

section VII) to help reduce the stress on the secondary components, is also demonstrated here experimentally. This was achieved by operating the prototype test rig with the secondary moving slowly across the primary pads in x-direction (with y-displacement=0mm) to check the handover of each primary system and the control action of the secondary electronics. Given the complete backbone system electronics (for the DCS system architecture) are still being developed, a Chroma power supply was used to supply the various primary inverters for this test, but this limited the power transfer capability due to its sensitivity to various transient changes. Consequently the validation was conducted with the secondary regulating 5kW to the output load at an output voltage of 300VDC.

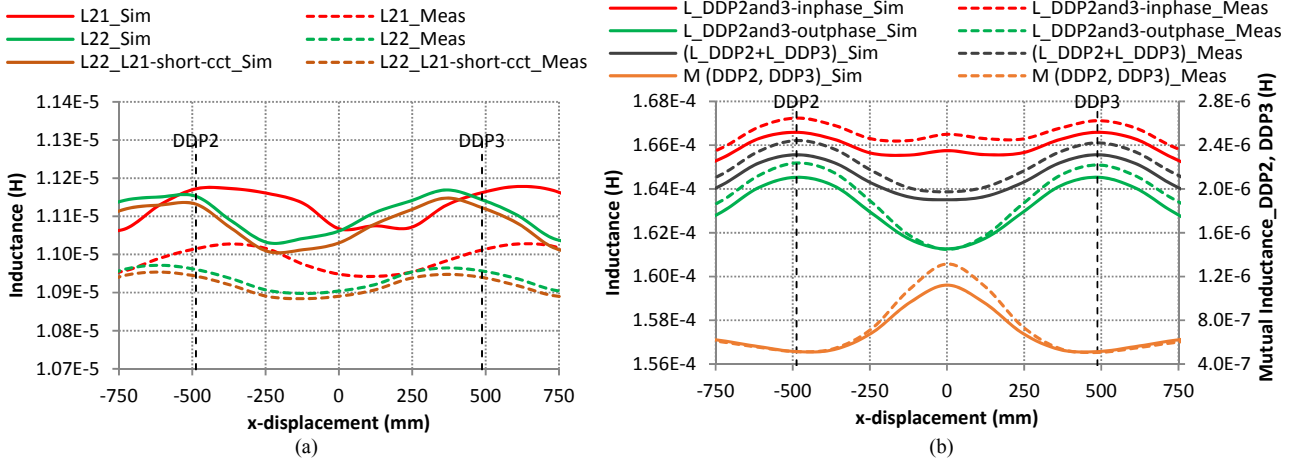


Fig. 12. Comparison between the simulated and measured values of the (a) secondary BPP coil inductances and (b) the inductance values of the primary DDPs

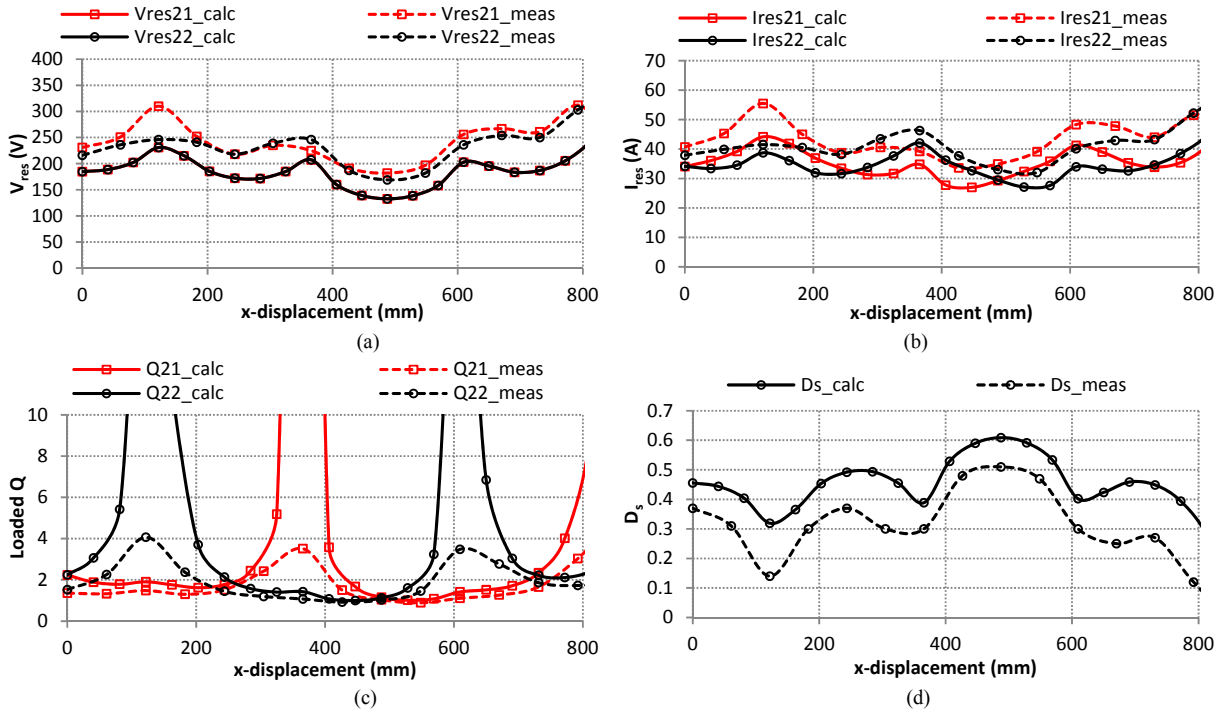


Fig. 13. Comparison between the calculated and measured values of the secondary (a) resonant voltages (b) resonant currents (c) operating Q s and (d) duty cycle of the regulator switch S ; as a function of secondary pad's displacement in x-direction (with y-displacement=0mm) for Ctrl1

The primary pads DDP 2 and 3 were energized in-phase w.r.t. each other with a current of 50A at 85kHz. The resultant values of secondary resonant voltages, currents and operating Q s along with the duty cycle (D_s) of the regulating switch S were recorded at discrete intervals along the secondary pads movement in x direction and are shown in Fig. 13 and 14. Here the calculated values for a system that is perfectly tuned and consists of ideal lossless components; are also shown for comparison. The equations given in [28] were used for these calculations, along with the simulated V_{oc} and I_{sc} values attained using 3D FEA tools. The results are shown with and without selective secondary coil decoupling (i.e., Ctrl2 and Ctrl1 operation respectively).

The results shown in Fig. 13 are for the secondary controller when it is operated under Ctrl1 mechanism (i.e., S3-S6 permanently open circuited), whereas, Fig. 14 shows the results Ctrl2 operation (i.e., S3-S6 used to selective decouple one of the BPP coils). The calculated and measured values show reasonably good agreement. The differences in these values can be attributed chiefly to the assumption of perfect tuning and ideal component characteristics for the calculated results. In addition the effects of imperfections of the built models and the imperfect alignment of the primary pads, minor differences in the actual and simulated relative positions of the primary and secondary pads, errors in self and mutual inductance values, and tolerances of measuring devices; are all compounded in the measured results presented here.

A comprehensive comparison of a BPP secondary used in a material handling application which also investigated Ctrl1 and Ctrl2 control strategies, was given in [28]. The scope of the work presented in this paper is limited only to highlighting

the fact that by implementing Ctrl2 scheme; the stress on the secondary regulator components can be reduced. However, for the results presented here, there are some operating points of particular interest which should be noted; including where there appears to be some larger discrepancies between simulation and practice.

As shown in Fig. 13 around x -displacement values of 120 and 610mm the BPP coil L_{22} fails to resonate up to the required Q value, whereas the BPP coil L_{21} fails to resonate up to the required value around x -displacement of 365mm. This is because around these points, the induced power in the respective secondary coils is too low (almost zero) to overcome the losses and effects of imperfect tuning of their resonant tanks; and hence fail to achieve their corresponding ideal calculated values of operating Q s required for power transfer. In Fig. 14, at x -displacement of around 245mm the BPP coil L_{21} is ideally able to support the load on its own, but as per the measured values both coils have to be employed in order to support the load at this position. This is because the ideal expressions which assume a perfectly tuned and lossless system show that the available power is only just sufficient for the load requirements as indicated by a very low D_s of around 7% in Fig. 14(d). In the practical system, the dimensional inaccuracies of the built models, component losses and imperfect tuning reduce the available power so that a single coil cannot support the load on its own. Consequently, when both coils operate to support the load, the additional power must be regulated, requiring an actual D_s of around 37% at this position. This condition is similar to that shown in Fig. 13(d) at the x -displacement of 245mm.

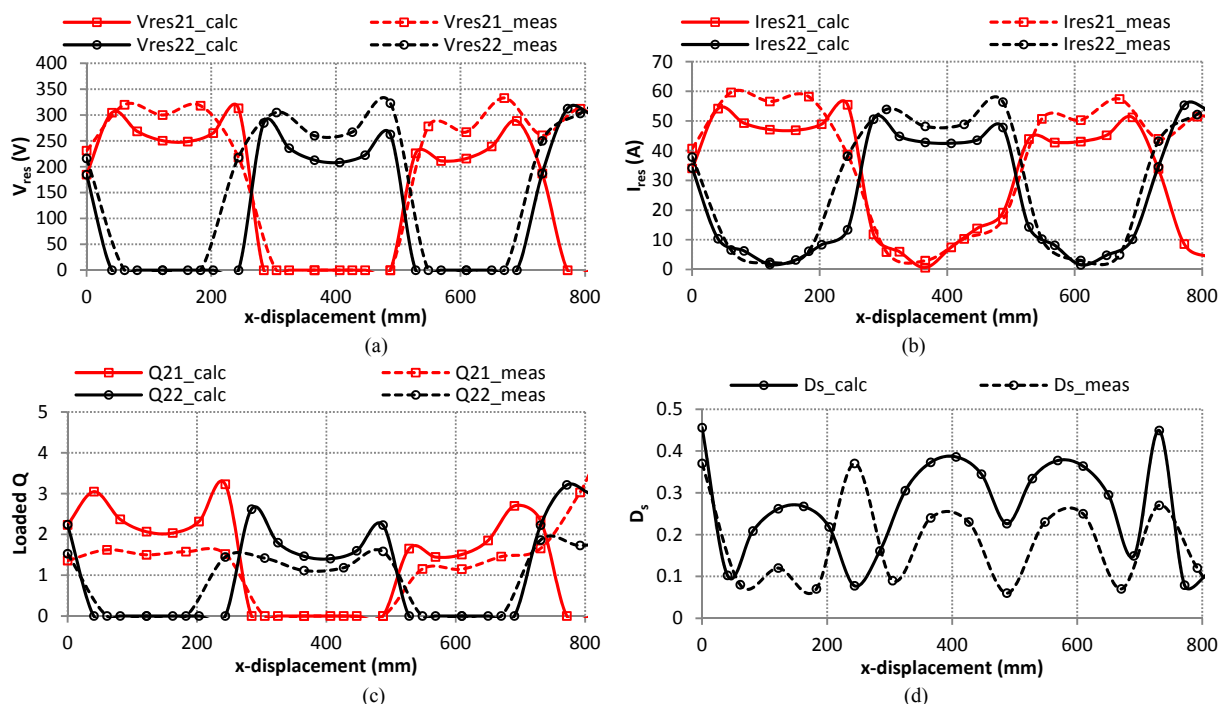


Fig. 14. Comparison between the calculated and measured values of the secondary (a) resonant voltages (b) resonant currents (c) operating Q s and (d) duty cycle of the regulator switch S ; as a function of secondary pad's displacement in x -direction (with y -displacement=0mm) for Ctrl2

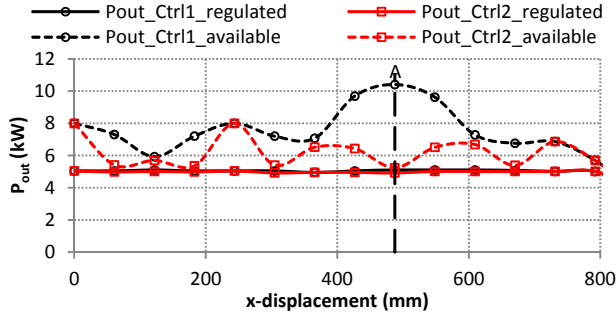
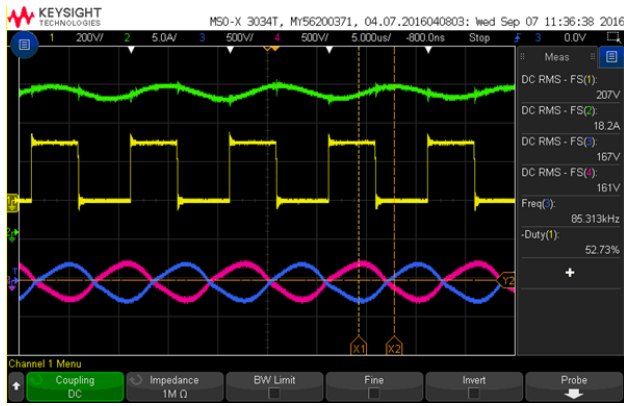
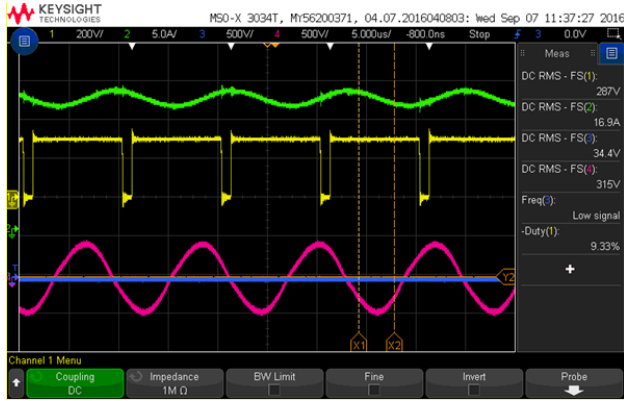


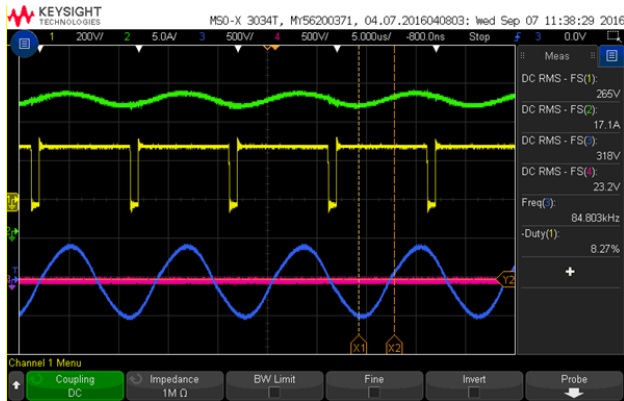
Fig. 15. Comparison of P_{out} and $P_{out_available}$ for the two control options i.e., Ctrl1 and Ctrl2



(a)



(b)



(c)

Fig. 16. Waveforms for V_s (Ch1 in yellow), I_{out} (Ch2 in green), V_{res21} (Ch3 in blue) and V_{res22} (Ch4 in magenta) at x -displacement = 487.5 mm (a) S3 to S6 all open circuited (b) S3 and S4 short circuited with S5 and S6 open (c) S5 and S6 short circuited with S3 and S4 open

In practice the measured D_s values are on average less than the calculated values for both control options, this is because the measured I_{sc} values are slightly lower than that simulated, with the available current to the rest of the system further reduced due to non-ideal tuning and losses in various components of the system (this further reduction is referred as I_{Δ} in [28]).

Figure 15 shows the value of P_{out} as a function of x -displacement under both control options. The power available at the input of the secondary regulator calculated using $P_{out_available} = P_{out}/(1 - D_s)$ is also shown here. This validates that when the secondary coils are selectively turned off in an appropriate manner as in Ctrl2 operation, the ratings of the circuit components need not be as high for a given output load requirement. This is an important consideration as it helps reduce the cost of the secondary electronics.

To further highlight the impact of the controller actions, oscilloscope captures are provided in Fig.16 when the secondary is positioned at the x -displacement = 487.5 mm (highlighted as point A in Fig.15). Here the BPP secondary is centrally aligned with the primary DDP3 and both the BPP coils can each provide the $P_{out} = 5kW$ required. Fig. 16 shows the waveforms for V_s , I_{out} , V_{res21} and V_{res22} at this position. As shown, if both coils are employed to support the load (i.e., Ctrl1; with S3-S6 all open circuited) $D_s = 52.73\%$, whereas when only one of the two coils is employed (i.e., Ctrl2) $D_s = 9.33\%$ and 8.27% respectively. Here a switching frequency of 100kHz is used for switch S.

IX. CONCLUSION

This paper detailed the magnetic design of a system capable of delivering 15kW of power to a moving vehicle continuously along the length of the track, while allowing a lateral misalignment of ± 200 mm from the centre of the track. The choice of primary and secondary pad topologies was made based on present options for stationary systems but focused on minimizing the cost of the in ground system by using a simple primary track topology. The use of a multicoin secondary enabled continuous power transfer while also demonstrating how such a system can help avoid rapid power pulses as the vehicle moves across the track.

The sizes of the primary and secondary pads proposed in this paper are suitable for an average car. The secondary (0.35m x 0.7m) is small enough to be installed underneath the car. In addition, the system is designed to deliver the power along the whole length of the track by energizing only one or maximum two adjacent primary pads at any given time. As the width of the primary pads is almost 1/3rd the width of an average car body. Whereas the combined length of two adjacent primary pads (including the gap between them i.e., $((0.775m \times 2) + 0.2m) = 1.75m$) is less than half the length of an average car. This means that under all operating conditions the energized primary pads are totally covered by the car body, which naturally lowers the exposure to leakage fields by providing a shielding effect.

The secondary side control action taken to help manage the

power flow to the load as the vehicle moves along the track is also demonstrated, while briefly highlighting the significance of detecting the position of the secondary pad for an effective primary side control.

REFERENCES

- [1] W. Yanzhen, A. P. Hu, D. Budgett, S. C. Malpas, and T. Dissanayake, "Efficient Power-Transfer Capability Analysis of the TET System Using the Equivalent Small Parameter Method," *IEEE Transactions on Biomedical Circuits and Systems*, vol. 5, pp. 272-282, 2011.
- [2] T. D. Dissanayake, A. P. Hu, S. Malpas, L. Bennet, A. Taberner, L. Booth, and D. Budgett, "Experimental Study of a TET System for Implantable Biomedical Devices," *IEEE Transactions on Biomedical Circuits and Systems*, vol. 3, pp. 370-378, 2009.
- [3] A. Abdolkhani and P. Hu, "Through-hole Contactless Slipping System based on Rotating Magnetic Field for Rotary Applications," *IEEE Transactions on Industry Applications*, vol. PP, pp. 1-1, 2014.
- [4] A. Abdolkhani and A. P. Hu, "A Contactless Slipping System Based on Axially Travelling Magnetic Field," *IEEE Journal of Emerging and Selected Topics in Power Electronics*, vol. PP, pp. 1-1, 2014.
- [5] J. Boys and A. Green, "Intelligent road-studs-lighting the paths of the future," in IPENZ Annual Conference 1996, Proceedings of: Engineering, providing the foundations for society; Volume 2; Papers presented in the technical programme of the IPENZ Annual Conference held in Dunedin, February 9-13, 1996, 1996, p. 169.
- [6] J. M. Barnard, J. A. Ferreira, and J. D. van Wyk, "Sliding transformers for linear contactless power delivery," *IEEE Transactions on Industrial Electronics*, vol. 44, pp. 774-779, 1997.
- [7] D. A. G. Pedder, A. D. Brown, and J. A. Skinner, "A contactless electrical energy transmission system," *IEEE Transactions on Industrial Electronics*, vol. 46, pp. 23-30, 1999.
- [8] P. Sergeant and A. Van den Bossche, "Inductive coupler for contactless power transmission," *IET Electric Power Applications*, vol. 2, pp. 1-7, 2008.
- [9] G. A. Covic and J. T. Boys, "Inductive Power Transfer," *Proceedings of the IEEE*, vol. PP, pp. 1-1, 2013.
- [10] S. Y. Hui, "Planar Wireless Charging Technology for Portable Electronic Products and Qi," *Proceedings of the IEEE*, vol. 101, pp. 1290-1301, 2013.
- [11] W. X. Zhong, X. Liu, and S. Y. R. Hui, "A Novel Single-Layer Winding Array and Receiver Coil Structure for Contactless Battery Charging Systems With Free-Positioning and Localized Charging Features," *IEEE Transactions on Industrial Electronics*, vol. 58, pp. 4136-4144, 2011.
- [12] W. X. Zhong, X. Lu, and S. Y. R. Hui, "Analysis on a Single-Layer Winding Array Structure for Contactless Battery Charging Systems with Free-positioning and Localized Charging Features," in *IEEE Energy Conversion Congress and Exposition*, Atlanta, 2010, pp. 658-665.
- [13] L. Nan and T. G. Habetler, "Design of a Universal Inductive Charger for Multiple Electric Vehicle Models," *IEEE Transactions on Power Electronics*, vol. 30, pp. 6378-6390, 2015.
- [14] M. R. Sonapreetha, S. Y. Jeong, S. Y. Choi, and C. T. Rim, "Dual-purpose non-overlapped coil sets as foreign object and vehicle location detections for wireless stationary EV chargers," in *Emerging Technologies: Wireless Power (WoW)*, 2015 IEEE PELS Workshop on, 2015, pp. 1-7.
- [15] J. M. Miller, O. C. Onar, and M. Chinthavali, "Primary-Side Power Flow Control of Wireless Power Transfer for Electric Vehicle Charging," *IEEE Journal of Emerging and Selected Topics in Power Electronics*, vol. 3, pp. 147-162, 2015.
- [16] S. Y. Choi, S. Y. Jeong, B. W. Gu, G. C. Lim, and C. T. Rim, "Ultraslim S-Type Power Supply Rails for Roadway-Powered Electric Vehicles," *IEEE Transactions on Power Electronics*, vol. 30, pp. 6456-6468, 2015.
- [17] S. Y. Choi, B. W. Gu, S. Y. Jeong, and C. T. Rim, "Advances in Wireless Power Transfer Systems for Roadway-Powered Electric Vehicles," *IEEE Journal of Emerging and Selected Topics in Power Electronics*, vol. 3, pp. 18-36, 2015.
- [18] J. M. Miller, O. C. Onar, C. White, S. Campbell, C. Coomer, L. Seiber, R. Sepe, and A. Steyerl, "Demonstrating Dynamic Wireless Charging of an Electric Vehicle: The Benefit of Electrochemical Capacitor Smoothing," *IEEE Power Electronics Magazine*, vol. 1, pp. 12-24, 2014.
- [19] S. Y. Choi, B. W. Gu, S. Y. Jeong, and C. T. Rim, "Trends of Wireless Power Transfer Systems for Roadway Powered Electric Vehicles," in *Vehicular Technology Conference (VTC Spring)*, 2014 IEEE 79th, 2014, pp. 1-5.
- [20] J. Meins and K. Vollenwyder, "System and method for transferring electric energy to a vehicle," United States Patent US8360216 B2, 2013.
- [21] S. Choi, J. Huh, W. Y. Lee, S. W. Lee, and C. T. Rim, "New Cross-Segmented Power Supply Rails for Roadway-Powered Electric Vehicles," *IEEE Transactions on Power Electronics*, vol. 28, pp. 5832-5841, 2013.
- [22] U. K. Madawala and D. J. Thrimawithana, "A Bidirectional Inductive Power Interface for Electric Vehicles in V2G Systems," *IEEE Transactions on Industrial Electronics*, vol. 58, pp. 4789-4796, 2011.
- [23] G. A. Covic and J. T. Boys, "Modern Trends in Inductive Power Transfer for Transportation Applications," *IEEE Journal of Emerging and Selected Topics in Power Electronics*, vol. 1, pp. 28-41, 2013.
- [24] A. Brooker, M. Thornton, and J. Rugh, "Technology Improvement Pathways to Cost-Effective Vehicle Electrification," National Renewable Energy Laboratory 2010.
- [25] G. Covic, J. Boys, M. Budhia, and C. Y. Huang, "Electric Vehicles-Personal transportation for the future," presented at the The 25th World Battery, Hybrid and Fuel Cell Electric Vehicle Symposium & Exhibition, Shenzhen, China, 2010.
- [26] M. Budhia, J. T. Boys, G. A. Covic, and H. Chang-Yu, "Development of a Single-Sided Flux Magnetic Coupler for Electric Vehicle IPT Charging Systems," *IEEE Transactions on Industrial Electronics*, vol. 60, pp. 318-328, 2013.
- [27] L. Chen, G. Nagendra, J. Boys, and G. Covic, "Double-Coupled Systems for IPT Roadway Applications," *IEEE Journal of Emerging and Selected Topics in Power Electronics*, vol. PP, pp. 1-1, 2014.
- [28] A. Zaheer, G. A. Covic, and D. Kacprzak, "A Bipolar Pad in a 10-kHz 300-W Distributed IPT System for AGV Applications," *IEEE Transactions on Industrial Electronics*, vol. 61, pp. 3288-3301, 2014.
- [29] A. W. Green and J. T. Boys, "10 kHz inductively coupled power transfer-concept and control," in *5th International Conference on Power Electronics and Variable-Speed Drives*, 1994, pp. 694-699.
- [30] O. H. Stielau and G. A. Covic, "Design of loosely coupled inductive power transfer systems," in *Proceedings International Conference on Power System Technology*, Perth, Australia, 2000, pp. 85-90.
- [31] A. Zaheer, M. Budhia, D. Kacprzak, and G. A. Covic, "Magnetic design of a 300 W under-floor contactless Power Transfer system," in *IECON 2011 - 37th Annual Conference on IEEE Industrial Electronics Society*, 2011, pp. 1408-1413.
- [32] G. A. Covic, J. T. Boys, A. M. W. Tam, and J. C. H. Peng, "Self tuning pick-ups for inductive power transfer," in *Power Electronics Specialists Conference*, Rhodes, 2008, pp. 3489-3494.
- [33] J. T. Boys, G. A. Covic, and Y. Xu, "DC analysis technique for inductive power transfer pick-ups," *IEEE Power Electronics Letters*, vol. 1, pp. 51-53, 2003.
- [34] A. Zaheer, H. Hao, G. A. Covic, and D. Kacprzak, "Investigation of Multiple Decoupled Coil Primary Pad Topologies in Lumped IPT Systems for Interoperable Electric Vehicle Charging," *IEEE Transactions on Power Electronics*, vol. 30, pp. 1937-1955, 2015.
- [35] A. Zaheer, D. Kacprzak, and G. A. Covic, "A bipolar receiver pad in a lumped IPT system for electric vehicle charging applications," in *IEEE Energy Conversion Congress and Exposition (ECCE)*, 2012, 2012, pp. 283-290.
- [36] G. Nagendra, G. Covic, and J. T. Boys, "Sizing of Inductive Power Pads for Dynamic Charging of EVs on IPT Highways," *Submitted to IEEE Transactions on Transportation Electrification*, vol. xx, pp. 1-8, 2016.
- [37] A. Zaheer and G. A. Covic, "A Comparative Study of Various Magnetic Design Topologies for A Semi-Dynamic EV Charging Application," in *Submitted to 2016 IEEE 2nd Southern Power Electronics Conference (SPEC)*, 2016, pp. 1-6.
- [38] K. Vollenwyder and J. Meins, "Producing electromagnetic fields for transferring electric energy to a vehicle," United States Patent US8544622 B2, 2013.
- [39] S. Y. Choi, J. Huh, W. Y. Lee, and C. T. Rim, "Asymmetric Coil Sets for Wireless Stationary EV Chargers With Large Lateral Tolerance by Dominant Field Analysis," *IEEE Transactions on Power Electronics*, vol. 29, pp. 6406-6420, 2014.
- [40] "Wireless Power Transfer for Light-Duty Plug-In/ Electric Vehicles and Alignment Methodology," ed: SAE TIR J2954\, 201605, 2016.
- [41] A. Kamini, M. Neath, A. Zaheer, and G. Covic, "Interoperable EV detection for dynamic wireless charging with existing hardware and free resonance," *Submitted to IEEE Transactions on Transportation Electrification*, vol. xx, pp. 1-8, 2016.



Adeel Zaheer received his B.Sc. degree in Electrical Engineering from the University of Engineering and Technology, Lahore, Pakistan, in 2007 and his PhD degree in Electrical and Electronic Engineering from the University of Auckland, New Zealand in 2015.

He is currently working as a Research Fellow at The University of Auckland, New Zealand. His research interests include inductive (contact-less) power transfer systems.



Michael J. Neath received the B.E. (Hons.) degree in electrical engineering and the Ph.D. degree from The University of Auckland, Auckland, New Zealand, in 2011 and 2015, respectively.

He is currently a Research Fellow with the University of Auckland. His current research interests include the fields of power electronics, wireless electric vehicle charging, and roadway-powered electric vehicles.



Hui Zhi (Zak) Beh (S'12-M'16) received his B.E. (Hons.), and PhD degrees in Electrical and Electronic Engineering from The University of Auckland, New Zealand in 2011 and 2016 respectively.

He is currently a Research Fellow at The University of Auckland. His research interests include the fields of power electronics, Inductive

Power Transfer (IPT) systems, wireless charging of electric vehicles and battery charging.



Grant A. Covic (S'88-M'89-SM'04) received his BE (Hons), and PhD degrees in Electrical and Electronic Engineering from The University of Auckland (UoA), New Zealand in 1986 and 1993 respectively. He was appointed as a full time Lecturer in 1992, a Senior lecturer in 2000, an Associate Professor in 2007 and to Professor in 2013 within the Electrical and Computer Engineering Department at the UoA, New Zealand. In 2010 he co-founded (with Prof. John Boys) a new global

start-up company "HaloIPT" focusing on electric vehicle (EV) wireless charging infrastructure, which was sold in late 2011. Presently he heads inductive power research at the UoA and co-leads the interoperability sub-team within the SAE J2954 wireless charging standard for EVs.

His research and consulting interests include power electronics, electric vehicle battery charging and highly resonant inductive (contact-less) power transfer (IPT) from which he has published more than 100 refereed papers in international journals and conferences. He holds a number of US patents with many more pending, from which licenses in specialized application areas of IPT have been granted around the world. He is a Fellow of the Institution of Professional Engineers New Zealand, a Fellow of the Royal Society of New Zealand, and (together with Prof. Boys) has been awarded the New Zealand Prime Ministers Science Prize, the KiwiNet Research Commercialisation Award, and the Vice Chancellors Commercialisation Medal for his work in IPT.